pubs.acs.org/Biomac

Article

Flotation Reagent Stress-Induced Extracellular Polymeric Substance Protein Secondary Structure in *Shewanella oneidensis* MR-1 Dictates the Morphology and Performance of Extracellular Polymeric Substance-Mediated ZnS Quantum Dots

Jingfeng Peng, Zuoyi Yang, Weifeng Song,* Wencan Dai,* Junming Bian, Weixiong Lin, Xiaohui Zhou, Keqin Zhou, Chuanying Tu, Guangwen Zheng, Ziheng Song, Xiangdan Zhang, and Xiaoyan Bai

Cite This: https://doi.org/10.1021/acs.biomac.6c00016

Read Online

ACCESS | Metrics & More | Article Recommendations | Supporting Information

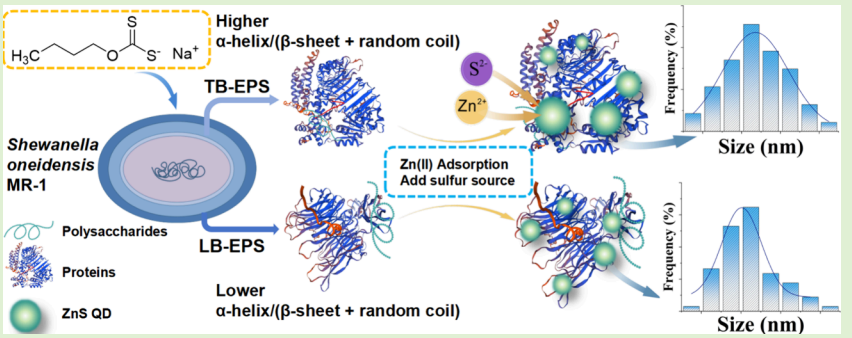

ABSTRACT: Extracellular polymeric substance (EPS)-mediated biosynthesis is a sustainable route for heavy metal valorization into quantum dots (QDs), yet how the EPS protein secondary structure regulates QD properties remains undefined. Herein, EPS from *Shewanella oneidensis* MR-1 cultivated under flotation reagent stress was utilized to synthesize high-performance ZnS QDs. Sodium butyl xanthate exhibited the optimal induction effect, significantly lowering the α-helix/(β-sheet + random coil) ratio in EPS. This structural shift promotes a more extended network, serving as a spatially ordered template for rapid, uniform ZnS nucleation. Analyzing QD materials mediated by distinct EPS layers (LB-EPS and TB-EPS) across treatments revealed strong correlations of this ratio with their size uniformity and specific surface area. Conversely, the QD yield and fluorescence intensity were governed primarily by chemical group abundance and synergistic structural−chemical factors, respectively. This dual regulatory mechanism demonstrates that manipulating the EPS protein structure is as crucial as modulating its chemical composition for nanomaterial biosynthesis.

1. INTRODUCTION

Zinc contamination generated during mining and mineral processing, particularly in lead−zinc flotation operations, poses serious threats to ecosystems and human health. Sodium butyl xanthate (SBX), sodium ethyl xanthate (SEX), and sodium diethyldithiocarbamate (DDTC) are among the most commonly used organic collectors in the flotation process, with the estimated world yearly use of these collectors being about 10^6 tons.[1] Residual flotation reagents in mining wastewaters are conventionally viewed merely as pollutants necessitating remediation.[2] However, from an alternative perspective, these reagents can be repurposed as "nongenetic regulators" that induce microorganisms to remodel the properties of their extracellular polymeric substances (EPS). This remodeling process provides unique biotemplates for the high-value valorization of heavy metals. *Shewanella oneidensis* MR-1 (*S. oneidensis* MR-1), a ubiquitous Gram-negative bacterium in mining environments, possesses a high Zn(II) tolerance and the ability to degrade xanthate pollutants. Thus, it serves as an ideal model system for this study.[3]

EPS is a complex mixture of biomacromolecules produced by microorganisms, primarily consisting of proteins, polysaccharides, nucleic acids, and lipids. EPS is rich in functional groups, including C=O, O−H, and N−H, which contribute to its strong metal adsorption and complexation capacities.[4] Critically, the inherent 3D architecture of these biomacromolecules provides a physical scaffold for metal ion capture and subsequent crystal

Received: January 4, 2026
Revised: April 16, 2026
Accepted: April 16, 2026
Published: April 23, 2026

growth. EPS may be grouped into loosely bound EPS (LB-EPS) and tightly bound EPS (TB-EPS), depending on their spatial density and binding properties. Due to variations in their molecular weight, composition, and spatial structure, these fractions exhibit distinct adsorption properties.[5,6] This inherent metal-immobilizing capability also opens a breakthrough in the valorization of heavy metals into functional nanomaterials using EPS.

Among these nanomaterials, metal sulfide quantum dots (MeS QDs, such as ZnS QDs) have received considerable attention because of their size-tunable fluorescence, wide bandgap, and great biocompatibility, which have broad application opportunities in bioimaging, optoelectronics, and sensing.[7] In this context, microbial synthesis of MeS QDs has emerged as a promising and sustainable nanomaterial production strategy, offering a green alternative to traditional chemical methods that often require high-energy input and involve toxic solvents.[8,9] Recent studies have predominantly focused on intracellular synthesis. For instance, metal-reducing bacteria such as *S. oneidensis* MR-1 can intracellularly synthesize MeS QDs by combining metal ions with S^{2-} derived from the reduction of sulfate or sulfite under anaerobic conditions[10] or with S^{2-} supplied from cysteine reduction under aerobic conditions.[11] However, intracellular methods often face challenges such as low yield per unit biomass and long reaction times (typically 12−96 h). Contrarily, an EPS-mediated synthesis is becoming popular as a cell-free variant. In this method, a stable biotemplate of extracellular QD formation is based on extracted EPS. This strategy provides multiple benefits such as improved QD size control,[12] higher production yield, and the avoidance of cytotoxicity, which permits higher metal concentrations.

Although EPS-mediated synthesis is an attractive strategy, its effectiveness is largely limited by factors such as the EPS yield, chemical composition, and structure. In existing research, common optimization strategies predominantly focus on modulating the chemical composition of EPS (e.g., enriching carboxyl or amino groups) to enhance metal ion uptake capacity.[13,14] However, this approach often overlooks a critical physical regulatory dimension. In fact, stress conditions can significantly regulate the protein secondary structure of EPS (e.g., rigid α-helix versus extended β-sheet), thereby determining the spatial arrangement of functional groups and directly serving as a physical template to regulate the nucleation process. Furthermore, significant secondary structural differences also exist between different EPS fractions (e.g., LB-EPS and TB-EPS).[15] Currently, there is a lack of systematic and in-depth understanding of how differences in EPS secondary structure influence the final properties of QDs and how to actively regulate these molecular architectures to achieve higher quality "burst nucleation".

Building on previous research findings,[3] this study investigates the use of EPS derived from *S. oneidensis* MR-1 under flotation reagent stress for the green synthesis of ZnS QDs, with a focus on the regulatory role of protein secondary structure in determining QD performance. The specific objectives were to (1) characterize changes in protein secondary structure and amino acid profiles of LB-EPS and TB-EPS induced by flotation reagent stress using circular dichroism (CD) spectroscopy and amino acid analysis; (2) evaluate the yield, optical properties, crystalline structure, particle size distribution, and specific surface area of ZnS QDs biosynthesized using stress-induced EPS fractions and clarify the influence of flotation reagent type and EPS spatial fraction (LB-EPS vs TB-EPS); (3) elucidate the structure−function relationship between EPS protein secondary structure and key QD performance metrics, including size uniformity, specific surface area, and fluorescence intensity. This work establishes a stressor-driven strategy for tailoring the EPS structure to produce high-performance ZnS QDs. This approach creates a synergistic pathway linking heavy metal remediation with the sustainable biosynthesis of nanomaterials, offering implications for environmental biotechnology and green nanotechnology.

2. MATERIALS AND METHODS

2.1. Materials

For *S. oneidensis* MR-1, Luria−Bertani medium composition and flotation reagent solutions were identical to those reported in the previous study.[3]

For sodium sulfide solution, a quantity of 0.39 g of anhydrous sodium sulfide solid was weighed, dissolved, and diluted to 100 mL with ultrapure water to obtain a 0.05 mol·L^{-1} sodium sulfide solution. This solution was used as the sulfur source for QD synthesis and was prepared fresh for immediate use.

2.2. Strain Activation and Stress Cultivation

All procedures for strain activation, glycerol stock preparation, and stress cultivation (including inoculum ratio of 5% v/v, incubation at 30 °C and 150 rpm, preculture duration of 48 h, main culture duration of 72 h, and flotation reagent concentrations of 0 to 300 mg·L^{-1}) followed exactly the protocols described in the previous publication.[3] This ensured complete consistency with the EPS samples characterized therein.

2.3. Extraction and Characterization of EPS

The LB-EPS was extracted using the thermal method, and TB-EPS was extracted via the NaOH method.[3] Briefly, cells were first harvested from the culture broth by centrifugation (2100*g*, 15 min, 4 °C). For LB-EPS extraction, the cell pellets were resuspended in 0.9% NaCl solution, incubated in a 60 °C water bath for 30 min, and then centrifuged (8000*g*, 15 min, 4 °C). The resulting supernatant was filtered through a 0.22 μm membrane to obtain LB-EPS. The remaining pellets were further utilized for TB-EPS extraction by resuspending them in 0.9% NaCl solution supplemented with 0.1 mL of 1 mol·L^{-1} NaOH. This mixture was incubated at 4 °C for 3 h, followed by identical centrifugation and filtration steps to collect TB-EPS. Finally, both EPS fractions were dialyzed (MWCO 4000 Da) against ultrapure water for 24 h to remove low-molecular-weight impurities before being stored at −20 °C.

For the present work, additional characterization focused on the protein secondary structure and amino acid profile was conducted on the same EPS samples. Protein secondary structure was analyzed by circular dichroism (CD) spectroscopy using 5 mL of EPS solution on a Jasco-815 spectrometer. Secondary structure content was calculated with CDNN software (version 1998).[16] Although CD deconvolution relies on standard protein databases and may face minor interference from nonproteinaceous chiral components in the heterogeneous EPS matrix, it is a well-established and highly sensitive method widely utilized in EPS research to accurately capture the relative conformational transitions of the dominant protein backbone.[17] Given that acid hydrolysis inevitably converts asparagine and glutamine into aspartic acid and glutamic acid, the previous study simply reported these total pools as Asp and Glu.[3] To ensure greater scientific rigor, the current analysis explicitly reports their combined values as Asx (Asp + Asn) and Glx (Glu + Gln). This precise classification provides deeper insights into how specific amino acid side chains contribute to stress-induced protein secondary structure reorganization.

2.4. Biosynthesis and Characterization of ZnS QDs

ZnS QDs were synthesized via EPS mediation as follows: 10 mL of 0.15 mol·L^{-1} Zn(II) solution ($ZnCl_2$, pH 4.0) was added to a 50 mL Erlenmeyer flask with 10.00 mg of freeze-dried EPS powder and diluted

https://doi.org/10.1021/acs.biomac.6c00016
Biomacromolecules XXXX, XXX, XXX−XXX

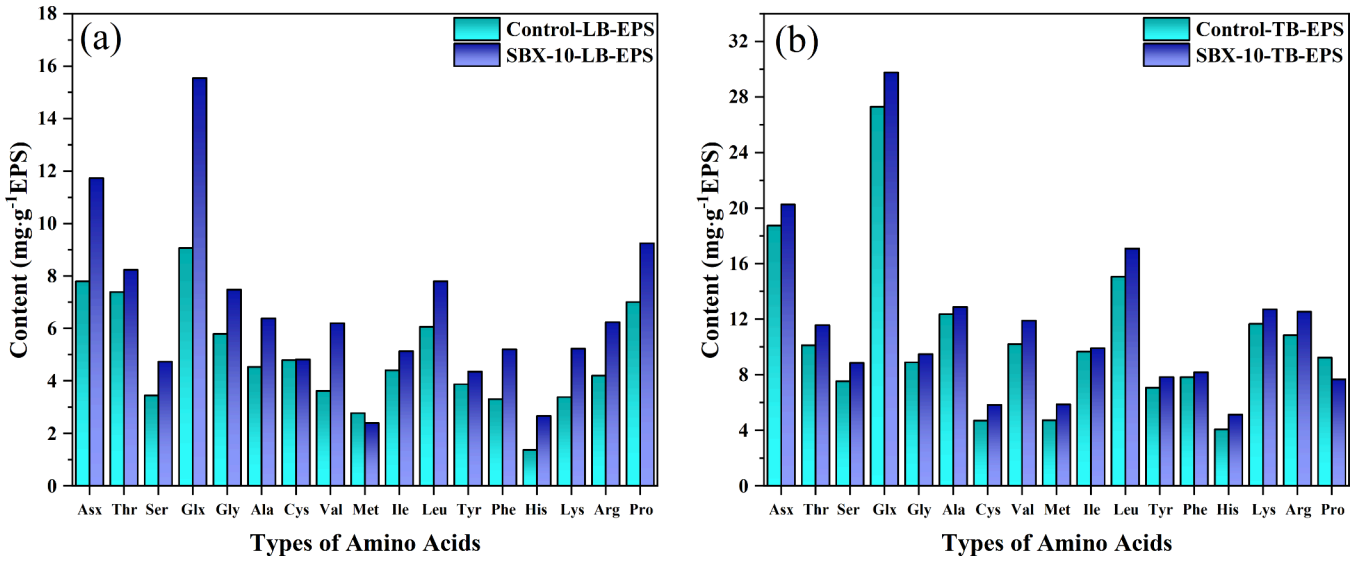

Figure 1. Amino acid information on (a) LB-EPS and (b) TB-EPS under SBX stress/induction (Asx = Asp + Asn; Glx = Glu + Gln).

to 20 mL with ultrapure water. The mixture was incubated at 30 °C with a shaking speed of 150 rpm (pH 5.0) for 120 min to allow Zn(II) binding to EPS functional groups.

The mixture was dialyzed (MWCO 4000 Da) in 200 mL of ultrapure water for 12 h to remove free metal ions. Afterward, 10 mL of 0.05 mol·L^{-1} S^{2-} solution (Na_2S) was slowly added dropwise, and the reaction proceeded for 30 min at room temperature to induce ZnS nucleation. The reaction mixture was first centrifuged at 6000*g* for 10 min at 4 °C to collect the raw precipitate. This precipitate was then alternately washed with ultrapure water and anhydrous ethanol for two complete cycles. The same centrifugation parameters were applied after each washing step, resulting in a total of five centrifugation cycles. The samples were freeze-dried and ground to powder for storage in a desiccator.

The concentration of free Zn(II) in the water phase was analyzed using atomic absorption spectroscopy, and the ZnS QD yield/unit EPS was determined. Various analyses were used to characterize the ZnS QDs further. Fourier transform infrared spectroscopy (FTIR, 4000−800 cm^{-1}) was utilized to identify functional groups, whereas X-ray diffraction (XRD, Bruker, Germany) was paired with Jade 9 software for phase identification. Transmission electron microscopy (TEM, JEM-F200, JEOL) was used to analyze the morphology and lattice structure. Lattice analysis was performed with Digital Micrograph 1.6.2, and particle size distribution was determined by using ImageJ. Elemental composition was examined by using scanning electron microscopy (SEM-EDS, MIRA LMS, TESCAN). Optical properties were investigated by using a steady-state/transient fluorescence spectrometer (FS5, Edinburgh Instruments). Thermal stability was evaluated through thermogravimetric analysis (TGA 550, TA) with a heating rate of 10 °C·min^{-1} under a N_2 atmosphere. Finally, the specific surface area and pore-size distribution were determined by Brunauer−Emmett−Teller (BET) analysis (ASAP 2460, Micromeritics).

2.5. Statistical Analysis

All experiments were performed in triplicate. Data are presented as the mean ± standard deviation (SD). Statistical analyses were conducted using an OriginPro 2021 (OriginLab, USA). Correlation analysis was performed using the linear fitting feature in OriginPro 2021.

3. RESULTS AND DISCUSSION

3.1. Impact of Flotation Reagents on EPS Production and Zn(II) Adsorption by *S. oneidensis* MR-1

As previously reported,[3] low-dose sodium butyl xanthate (SBX, 10 mg·L^{-1}) induced the strongest stress response in *S. oneidensis* MR-1, resulting in the highest yield of both LB-EPS and TB-EPS together with the greatest Zn(II)-binding capacity. A higher concentration of sodium ethyl xanthate (SEX, 200 mg·L^{-1}) produced the second-highest EPS yield and Zn(II) adsorption performance, whereas sodium diethyldithiocarbamate (DDTC, 50 mg·L^{-1}) showed the weakest induction effect among the three reagents. Accordingly, EPS samples from these optimal stress conditions (SBX-10-LB/TB-EPS, SEX-200-LB/TB-EPS, and DDTC-50-LB/TB-EPS) along with untreated Control-LB/TB-EPS were selected for subsequent ZnS QD biosynthesis and detailed structural characterization.

3.2. Characterization of *S. oneidensis* MR-1 EPS under Different Flotation Reagent Stress/Induction

3.2.1. FTIR and XPS Analysis of EPS Before and After Flotation Reagent Stress/Induction. FTIR and XPS analyses of the EPS samples confirmed that 10 mg·L^{-1} SBX stress significantly enriched oxygen- and nitrogen-containing functional groups (C=O, C−O/C−N, C=N, N−H, and −COOH) in both LB-EPS and TB-EPS, as reported in detail in the previous study.[3] These changes provided more Zn-binding sites and served as the chemical foundation for the subsequent QD biosynthesis.

3.2.2. Amino Acid Analysis of EPS Before and After Stress/Induction. The amino acid compositions of the control groups (Control-LB-EPS and Control-TB-EPS) and optimally stressed groups exhibiting the highest adsorption capacities (SBX-10-LB-EPS and SBX-10-TB-EPS) were analyzed by an amino acid analyzer. Before detailing these profiles, it is worth noting that while EPS is a heterogeneous mixture containing both proteins and polysaccharides, this study predominantly focuses on the protein component. This is primarily because proteins constitute the overwhelming majority (approximately 68.1−95.9%) of the EPS mass in the SBX-stressed and the control groups, as detailed in the preceding work.[3] Nevertheless, the role of polysaccharides should not be overlooked; they are rich in −OH groups, which act as vital auxiliary binding sites contributing to the initial electrostatic trapping of Zn(II) ions.[18] However, given their significantly lower mass fraction, their structural templating contribution is likely secondary to that of the dominant protein component.

As shown in Figure 1, Asx (Asp/Asn) and Glx (Glu/Gln) were dominant in EPS and accounted for more than 30% of the total amino acid content. SBX stress greatly enhanced the

https://doi.org/10.1021/acs.biomac.6c00016
Biomacromolecules XXXX, XXX, XXX−XXX

relative abundance of Asx and Glx in LB-EPS by 50.6% and 71.5%, respectively, indicating that the composition of EPS proteins was significantly regulated after stress. Asp and Glu are both acidic amino acids with terminal −COOH groups that can act as electron donors to form coordination bonds with transition metal ions[19] and are thus considered as main sites for metal−EPS interactions. Asn and Gln contain amide groups ($-CONH_2$) on their side chains, which further enhance this coordination potential.[20] Therefore, the concurrent increase in Asx and Glx contents contributed additional −COOH and C=O/C−N sites, explaining the significant improvement in metal-binding capacity. The collective enrichment of these acidic and amide amino acids, providing abundant −COOH from Asp/Glu and amide C=O from Asn/Gln, strongly aligns with the enhanced C=O/−COOH peaks observed in the XPS O 1s spectra.[3]

Furthermore, changes in amino acid composition provide an explanation for the significant increase in the C−N component observed in the XPS C 1s spectra.[3] Specifically, the enrichment of Asn and Gln contributes an abundance of amide C−N bonds. Concurrently, the substantial increase in the content of basic amino acids (His, Lys, and Arg) also contributes to C−N bonds. Whether through the $-CONH_2$ of the amide amino acids or the additional $-NH_2$ groups within the side chains of the basic amino acids, both exhibit strong chelating capabilities toward heavy metals. Among the basic amino acids, the imidazole C=N groups of His demonstrate a strong affinity for heavy metals;[21] this observation aligns with the enhanced C=N signal detected in the XPS N 1s spectra.[3] Lys and Arg may also facilitate the immobilization of metals and the aggregation of EPS through electrostatic interactions and hydrogen bonding.[22] Consequently, the synergistic upregulation of these nitrogen-rich amino acids directly results in a macroscopic increase in the C−N/C=N content within the EPS, thereby enhancing the Zn(II) adsorption capacity of the EPS.

Overall, SBX stress leads to a marked increase in acidic, amide, and basic amino acids, thereby strengthening the coordination capacity of the EPS. The resulting constellation of functional groups promotes the robust adsorption and stabilization of metal ions, providing the chemical groundwork necessary for achieving a high ZnS QD yield. Alongside these compositional changes, the altered amino acid profile drives a notable restructuring of the protein framework: EPS proteins begin to unfold, exposing previously buried domains and adopting a more flexible extended conformation. This transition in the protein architecture emerges as the central physical factor governing the templated nucleation pathway. Its contribution becomes clearer in the following text where circular dichroism spectroscopy is employed to quantify the associated structural shifts.

3.2.3. Changes in Protein Secondary Structure of EPS Before and After Stress/Induction. The CD spectra of Control-LB-EPS, SBX-10-LB-EPS, Control-TB-EPS, and SBX-10-TB-EPS are shown in Figure 2, revealing clear spectral deviations after SBX stress that point to substantial reorganization of the EPS protein architecture. Corresponding secondary structure quantification (Table 1) highlights this shift: in LB-EPS, the α-helix fraction declines from 7.7% to 6.6%, whereas the β-sheet fraction shows a modest rise from 40.4% to 42.1%. TB-EPS undergoes an even more pronounced transition, with α-helix content dropping from 13.2% to 8.2% and β-sheet content increasing from 35.8% to 39.7%. The proportions of β-turns and random coils remain comparatively steady, suggesting that the

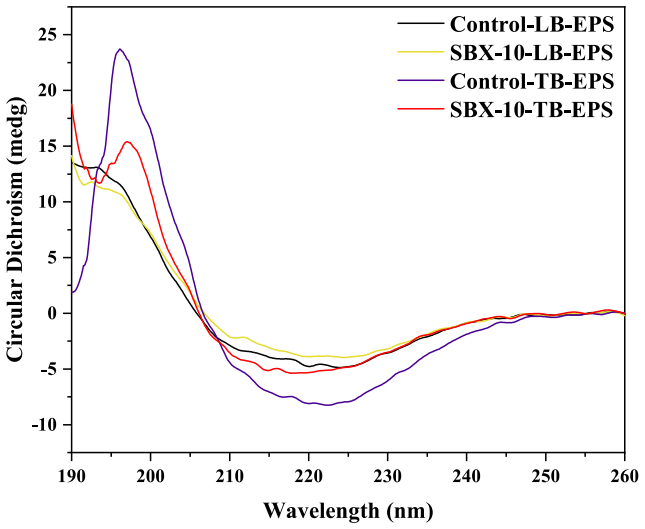

Figure 2. Circular dichroism (CD) spectrum of EPS.

Table 1. Changes in the Secondary Structure of Proteins in LB-EPS and TB-EPS Before and After SBX Stress/Induction

	secondary structures				
EPS type	α-helix	β-sheet	β-turn	random coil	α-helix/ (β-sheet + random coil)
Control-LB-EPS	7.7%	40.4%	17.5%	34.9%	0.1022
SBX-10-LB-EPS	6.6%	42.1%	17.0%	34.3%	0.0865
Control-TB-EPS	13.2%	35.8%	16.0%	35.2%	0.1859
SBX-10-TB-EPS	8.2%	39.7%	17.4%	34.8%	0.1101

most significant redistribution occurs between α-helix and β-sheet populations. Such conformational alteration, from the rigid α-helix to the extended β-sheet, can be connected with the alterations in amino acid compositions that are observed in Section 3.2.2. According to Chou−Fasman predictive parameters,[23] the β-sheet propensities [P(β)] of the amide-containing amino acids (Asn: 89 and Gln: 110) and basic amino acids (Arg: 93, His: 87, and Lys: 74) are significantly higher than Asp (54) and Glu (37). Though the amino acid analysis measured the acidic and amide residues combined as Asx and Glx, the pronounced transition toward β-sheet structures strongly suggests that SBX stress specifically drove a higher proportional incorporation of Asn and Gln within these combined pools. The $-CONH_2$ of Asn and Gln together with the nitrogen-rich functional groups of the basic residues readily participate in robust intermolecular hydrogen-bonding networks and electrostatic interactions. This thermodynamically favors the formation of β-sheet structures. The observed rise in the level of β-sheet is therefore a synergistic amplification of these particular high-P(β) amino acids as a result of the action of SBX stress.

To quantify the overall flexibility of the protein, the α-helix/(β-sheet + random coil) ratio was introduced and calculated.[15] A decrease in this ratio can reflect a transition of the protein from a compact conformation to a more loose and extended conformation. Under SBX stress, this ratio decreases from 0.1022 to 0.0865 in LB-EPS and from 0.1859 to 0.1101 in TB-EPS, confirming that SBX exposure promotes substantial structural loosening. The observed increase in β-sheet content implies the formation of an extended backbone hydrogen-bond

https://doi.org/10.1021/acs.biomac.6c00016
Biomacromolecules XXXX, XXX, XXX−XXX

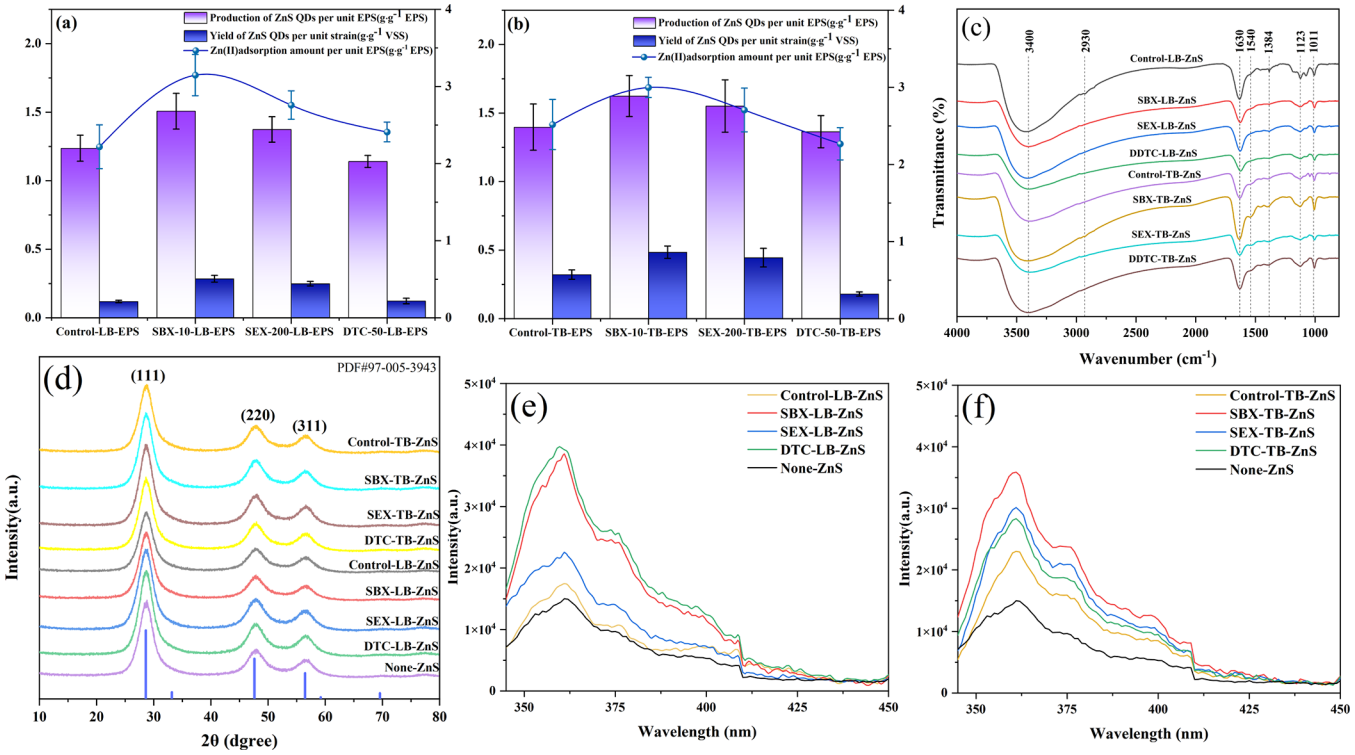

Figure 3. Adsorption properties of (a) LB-EPS and (b) TB-EPS on Zn(II) under stress/induction and ZnS QDs yields. (c) FTIR, (d) XRD patterns, and PL fluorescence of (e) LB-ZnS and (f) TB-ZnS. Note: PL fluorescence excitation at 295 nm. No discrete XRD peaks for EPS are observed in panel (d) due to its inherent amorphous nature.

network that likely facilitates protein self-assembly into a more pliable, mesh-like supramolecular scaffold.[24] Such an unfolded ligand framework is highly relevant to biomineralization as it creates a spatially ordered template for nucleation. By freeing the main-chain C=O and N−H groups from the intramolecular hydrogen bonds that stabilize the α-helix and by aligning polar side chains more uniformly along the protein backbone, the conformational shift produces an accessible and orderly coordination environment.[25] Among the examined samples, SBX-10-LB-EPS exhibits the lowest α-helix/(β-sheet + random coil) ratio (0.0865), indicating the most extensively unfolded and flexible conformation. This structural feature of LB-EPS not only facilitates rapid ion diffusion and immobilization but also foreshadows its superior capability in regulating nucleation uniformity compared to the more rigid TB-EPS, a hypothesis validated by the QD characterization in subsequent sections.

3.3. EPS-Mediated Synthesis of ZnS QDs under Flotation Reagent Stress

The effects of EPS extracted under different flotation reagent stress-induction conditions on the synthesis of ZnS QDs were investigated. ZnS QDs synthesized with LB-EPS and TB-EPS extracted under optimal stress concentrations were designated as SBX-LB/TB-ZnS, SEX-LB/TB-ZnS, and DDTC-LB/TB-ZnS. The control groups synthesized using unstressed LB-EPS and TB-EPS were denoted as Control-LB/TB-ZnS. Chemically synthesized ZnS (without EPS) was designated as None-ZnS.

3.3.1. Yield, XRD, FTIR, and PL Analyses of ZnS QDs. The yield of ZnS QDs and the equilibrium adsorption capacity of Zn(II) were evaluated under different EPS-mediated conditions. As shown in Figure 3a,b, the yields of ZnS QDs varied significantly following flotation reagent stress. SBX-10-EPS and SEX-200-EPS markedly enhanced QD production, with SBX-stressed EPS being the most effective. Specifically, SBX-10-LB-EPS and SBX-10-TB-EPS yielded 1.51 g·g^{-1} EPS and 1.62 g·g^{-1} EPS, representing increases of 21.83% and 16.23% compared with the controls, respectively. In contrast, DDTC-50-EPS-mediated synthesis resulted in reduced yields, with LB-EPS and TB-EPS producing 1.14 g·g^{-1} EPS and 1.36 g·g^{-1} EPS, corresponding to decreases of 7.82% and 2.49%, respectively. After normalization to cell dry weight (VSS), the ZnS QD yield per unit LB-EPS under SBX stress was 0.484 g·g^{-1} VSS, a 140.68% increase. The yield per unit TB-EPS was 0.284 g·g^{-1} VSS, a 50.78% increase (the cell dry weight results are detailed in the previous study[3]). Furthermore, SBX-10-LB-EPS and SBX-10-TB-EPS exhibited equilibrium Zn(II) adsorption capacities of 3.14 g·g^{-1} EPS and 3.00 g·g^{-1} EPS, respectively, representing 41.90% and 19.17% increases over the controls.

Although SBX-10-LB-EPS had a greater equilibrium Zn(II) adsorption capacity compared with SBX-10-TB-EPS, the QD yield of SBX-10-LB-EPS was lower. To explain this phenomenon, the concentration of Zn(II) in the supernatant was determined following the first, second, and fourth centrifugation cycles in the washing of SBX-LB-ZnS and SBX-TB-ZnS (see Figure S1 in the Supporting Information). Higher Zn(II) concentrations were detected in the supernatant of SBX-LB-ZnS, suggesting that Zn(II) bound to LB-EPS was more easily released. This indicates that although LB-EPS is capable of adsorbing high concentrations of Zn(II), the interaction mainly relies on weak forces, thus causing higher desorption or loss of ZnS QDs during the washing process. In contrast, TB-EPS, which is rich in high-molecular-weight components, presumably forms more effective coordination with heavy metals,[26,27] which stabilizes the QDs. Thus, the capacity of EPS adsorption and the binding strength do not always have a positive correlation.

https://doi.org/10.1021/acs.biomac.6c00016
Biomacromolecules XXXX, XXX, XXX−XXX

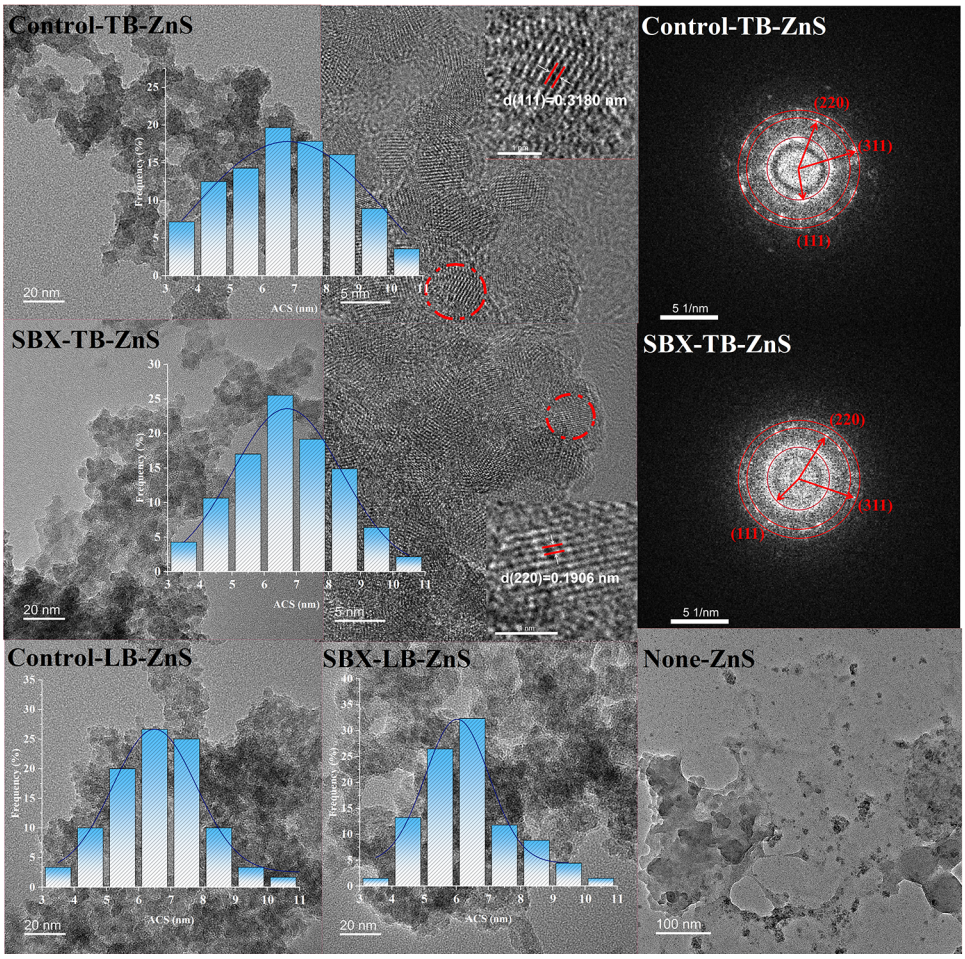

Figure 4. TEM images of Control-LB-ZnS, SBX-LB-ZnS, Control-TB-ZnS, SBX-TB-ZnS, and None-ZnS. HRTEM and diffraction ring images were generated by Digital Micrograph 1.6.2 of Control-TB-ZnS and SBX-TB-ZnS.

Figure 3c shows the FTIR spectra of the synthesized ZnS. The characteristic absorption bands were similar to those of EPS, which validated the participation of EPS in QD synthesis (the FTIR spectra of EPS can be found in the previous study.[3]). The ZnS spectra, however, had redshifts at 3440 cm^{-1}, 1645 cm^{-1}, 1546 cm^{-1}, 1400 cm^{-1} and 1054 cm^{-1}, the loss of the 1241 cm^{-1} band, and the appearance of a new peak at 1123 cm^{-1}, as compared with the EPS spectra. Changes in the vibrational frequencies of these C=O, O−H, N−H, and C−N functional groups indicate their involvement in complexing or coordinating with Zn(II).[28,29] The appearance of the new band likely reflects the binding of certain EPS functional groups to the ZnS surface, forming new vibrational modes. Specifically, the significant shift at 1645 cm^{-1} (amide I band) strongly indicates that the main-chain C=O groups of the protein played a critical role in the Zn(II) coordination and subsequent nucleation process. This observation provides direct molecular-level evidence for the main-chain group liberation discussed in the later conformational templating mechanism.

Figure 3d displays the XRD patterns. Compared with the standard reference card PDF#97-005-3943, three distinct diffraction peaks were observed at 2θ values of 28.53°, 47.73°, and 56.64°, corresponding to the (111), (220), and (311) planes, respectively. These are the main peaks of ZnS, which validates the existence of cubic β-ZnS.[30] There were no observed peak shifts, which suggested that the EPS-mediated synthesis yielded highly uniform crystal phases. It is worth noting that although the FTIR results of ZnS QDs confirmed the tight binding of EPS to ZnS, no diffraction peaks corresponding to the EPS component were observed in the XRD pattern. This is attributed to the inherent amorphous nature of the EPS as a biomacromolecule.[31]

The PL spectra (Figure 3e,f) showed a strong emission peak at 361 nm for the ZnS QDs. It is noteworthy that the EPS-mediated ZnS QDs exhibited a stronger fluorescence intensity than the None-ZnS, with a further enhancement observed after flotation reagent stress. This variation is associated with the abundance, size uniformity, and dispersion state of the QDs within the material,[13,32,33] which will be discussed in detail in Sections 3.3.2−3.3.4.

3.3.2. TEM, HRTEM, and SEM-EDS Analyses of ZnS QDs. The particle size distribution, lattice spacing, and diffraction rings of ZnS QDs were analyzed by using TEM and HRTEM combined with relevant software. As shown in Figure 4, the TEM image (scale bar: 20 nm) revealed that the EPS-mediated ZnS QDs were primarily attached to the EPS macromolecular structures. This was attributed to the fact that the EPS adsorbed Zn(II) ions, and after the introduction of a sulfur source, the QDs were formed on the functional groups of the EPS.

The HRTEM images (scale bar: 5 nm) showed nearly spherical ZnS QDs with distinct boundaries, uniform distribution, and good crystallinity. Particle size statistics obtained using ImageJ indicated average sizes (ACS) of 6.63 ± 1.46 nm for

https://doi.org/10.1021/acs.biomac.6c00016
Biomacromolecules XXXX, XXX, XXX−XXX

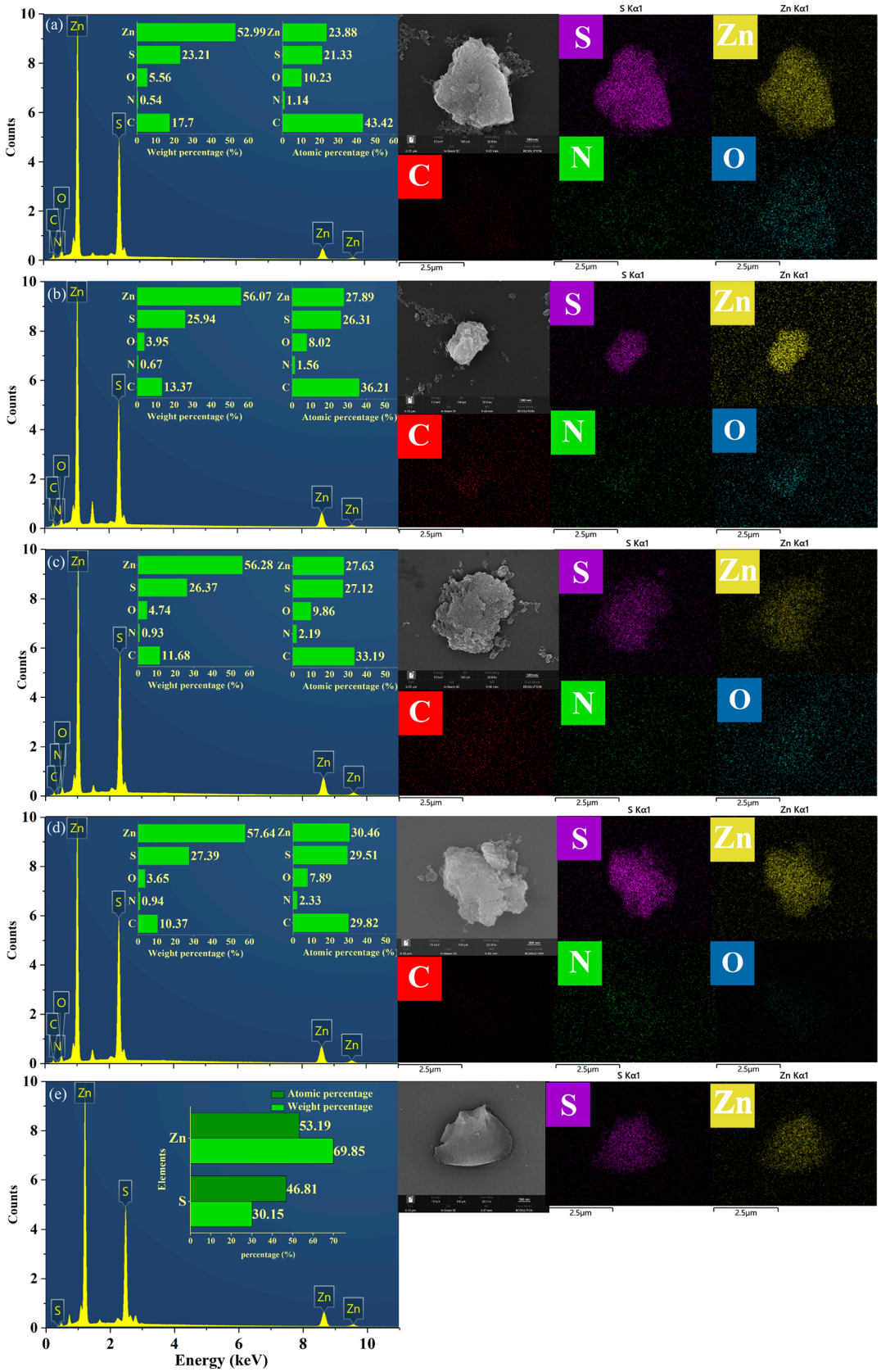

Figure 5. SEM-EDS profiles of (a) Control-LB-ZnS, (b) SBX-LB-ZnS, (c) Control-TB-ZnS, (d) SBX-TB-ZnS, and (e) None-ZnS, alongside the corresponding EDS elemental mapping images of C, N, O, Zn, and S.

Control-LB-ZnS, 6.44 ± 1.37 nm for SBX-LB-ZnS, 6.81 ± 1.85 nm for Control-TB-ZnS, and 6.67 ± 1.60 nm for SBX-TB-ZnS, all within the QD size range (<20 nm). To provide a quantitative scientific definition of size uniformity, the statistical polydisper-

https://doi.org/10.1021/acs.biomac.6c00016
Biomacromolecules XXXX, XXX, XXX−XXX

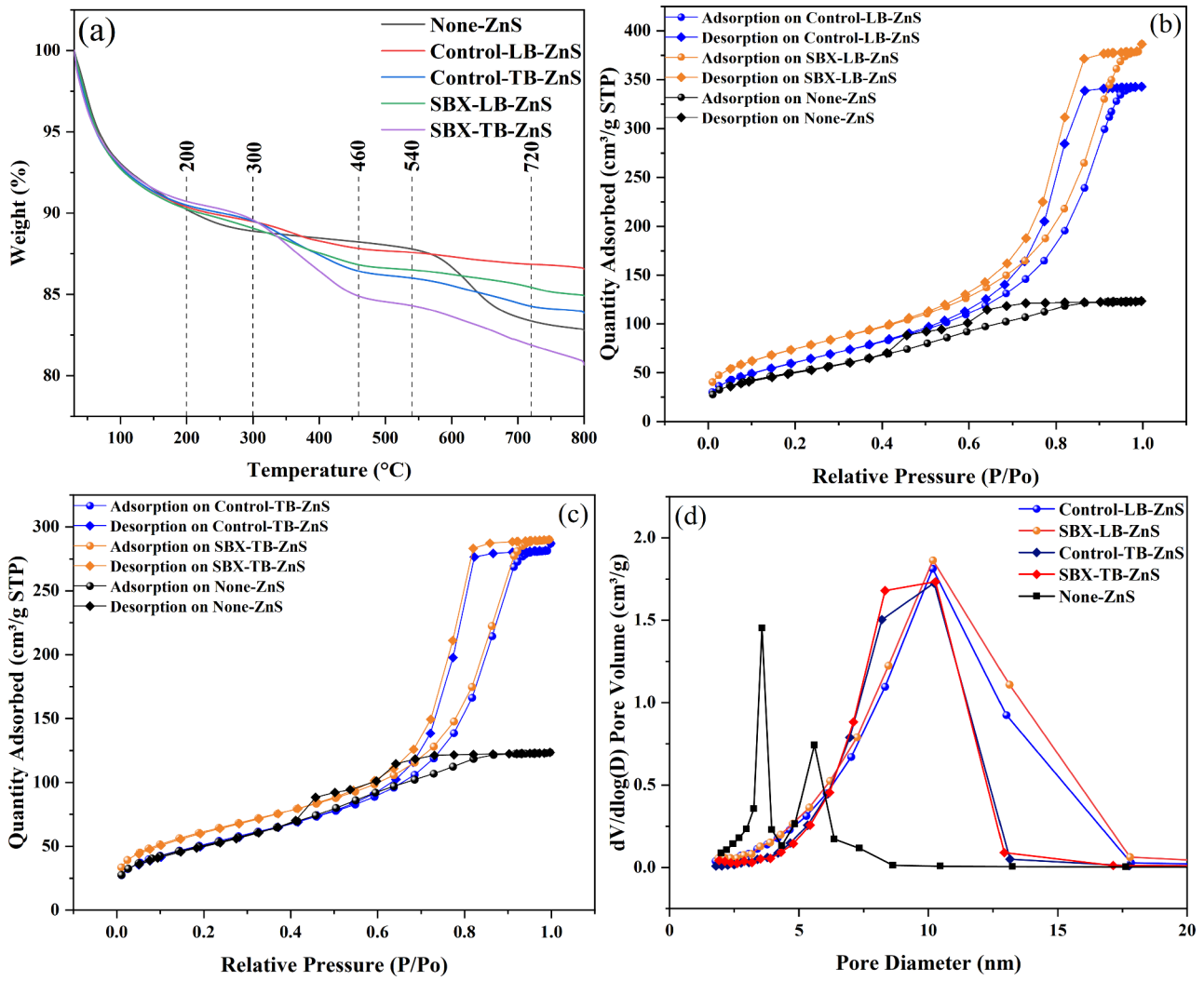

Figure 6. (a) TGA, (b) N_2 adsorption−desorption curves (degassing temperature: 300 °C) of LB-ZnS, (c) TB-ZnS, and (d) pore-size distribution.

sity index (PDI = $(\sigma/\mu)^2$, where σ is the standard deviation of the particle size distribution (nm) and μ is the mean particle size (nm)), was calculated based on the TEM size distribution data. The results showed that the SBX-induced groups possessed lower PDI values (SBX-LB-ZnS: PDI = 0.045; SBX-TB-ZnS: PDI = 0.058) compared to their respective controls (Control-LB-ZnS: PDI = 0.048; Control-TB-ZnS: PDI = 0.074). This mathematically confirms that the particle size distribution of SBX-LB-ZnS and SBX-TB-ZnS was significantly more concentrated. In contrast, the None-ZnS sample synthesized without EPS as a template exhibited a highly nonuniform particle size distribution, with large particles exceeding 50 nm. The TEM results further explain the PL findings in Section 3.3.1 by directly visualizing the particle size distribution. Since a broader size distribution is a known critical factor for increasing defects and reducing fluorescence intensity in QDs,[33] the superior uniformity observed in these EPS-mediated QDs provides a direct explanation for the enhanced PL.

ZnS in the presence of EPS had a significantly better size uniformity than None-ZnS, which was due to the stabilizing effect of EPS throughout the synthesis. As discussed above, functional groups such as C=O and N−H are also capable of inducing adsorption of Zn(II) ions, which provide nucleation sites and subsequently control ZnS QD growth when the sulfur sources are introduced. This controlled nucleation and growth process efficiently prevented excessive particle enlargement, resulting in smaller, uniformly distributed nanoparticles. This mechanism is similar to that described by Soltani et al.,[34] where polyvinylpyrrolidone was used as a capping reagent to make ZnS nanoparticles small and uniform. Likewise, the high concentration of functional groups in EPS might have enabled QD nucleation by taking place via steric hindrance and electrostatic stabilization. Furthermore, SBX-LB-ZnS and SBX-TB-ZnS displayed narrower particle size distributions, which may be attributed to stress-induced changes in protein secondary structures that exposed additional binding sites and enhanced the reactivity of functional groups, as will be discussed in Section 3.3.4.

To further verify the data obtained during the XRD analysis, the Electron Diffraction Tools plugin of Digital Micrograph 1.6.2 was employed to carry out FFT analysis of the HRTEM images. To measure fine lattice spacings, Gaussian filtering and autocorrelation were used to optimize ring diffraction. These findings confirmed the high crystallinity of EPS-based ZnS QDs; the distinct interplanar spacings of 0.3180 nm for ZnS (111) and 0.1906 nm for ZnS (220) aligned with the XRD results. The presence of multiple diffraction spots forming concentric rings indicated an isotropic polycrystalline structure.[35]

https://doi.org/10.1021/acs.biomac.6c00016
Biomacromolecules XXXX, XXX, XXX−XXX

SEM-EDS analysis (Figure 5) confirmed the elemental composition of the synthesized QDs. The measured Zn:S atomic ratios across all samples were approximately 1:1, aligning with the stoichiometry of ZnS. QDs synthesized from SBX-stressed EPS (both LB and TB fractions) showed an atomic percentage of Zn higher than those of their controls, accounting for the greater abundance of ZnS QDs observed. This finding directly explains the enhanced fluorescence intensity recorded after SBX stress.[32] The higher Zn content in SBX-TB-ZnS compared to that in SBX-LB-ZnS was consistent with the respective QD yields. Furthermore, the presence of C, N, and O elements in all EPS-mediated samples verified the incorporation of EPS biomacromolecules into the final QD product.[14]

To further validate the adsorption and nucleation behavior of EPS on the QDs, the EDS elemental mapping results for C, N, O, Zn, and S are listed in Figure 5. The strong Zn and S signals distinctly delineate the inorganic nanoparticle cores. The distributions of C, N, and O, which originate from the EPS biomacromolecules, appear spatially uniform and closely coincide with the Zn and S signals. This clear overlap provides direct visual confirmation that the EPS matrix adsorbs onto and homogeneously encapsulates the ZnS QDs. As an effective biological coating, EPS is capable of stabilizing nanocrystals and maintaining their structural integrity.

3.3.3. TG and BET Analyses of ZnS QDs. TG analysis was used to analyze the thermal stability of Control-LB-ZnS, SBX-LB-ZnS, Control-TB-ZnS, SBX-TB-ZnS, and None-ZnS (Figure 6a). Between 30 and 200 °C, there was a total of about 10% of weight loss in all the samples, likely due to the evaporation of absorbed or structural water.[36] This suggests that the thermal stability of the ZnS QD core structure was maintained, as the weight loss was attributable solely to the removal of physisorbed water. The weight loss of 2.23−5.16% at 300−460 °C was observed among the four EPS-mediated synthesis samples, which was primarily due to the thermal degradation of EPS proteins and polysaccharides.[37] At 540−720 °C, further decomposition of protein and polysaccharide residues containing carbonaceous compounds took place and led to further weight losses of 0.72−2.41%. Above 720 °C, Control-LB-ZnS, SBX-LB-ZnS, and Control-TB-ZnS stabilized with residual weights of 84.90−86.55%. Nonetheless, SBX-TB-ZnS continued to lose mass, resulting in a residual mass of 80.67%. This can be attributed to the fracture of the framework and the collapse of mesoporous structures at high temperatures.[38] Conversely, the mass decrease pattern in the None-ZnS samples was limited in 540−720 °C, which led to a 4.43% loss. The same was not the case with a range of 300−460 °C. The remaining residual mass of the sample was 82.77%.

In summary, the residual mass of EPS-ZnS composites (80.67−86.55%) was comparable to that of None-ZnS (82.77%). Crucially, the distinct, multistep degradation profile, particularly the significant mass loss observed in the 300−460 °C range, confirms the formation of a robust bioinorganic hybrid structure. Such behavior indicates that EPS macromolecules wrap tightly around the ZnS cores, functioning as stabilizing ligands that maintain both dispersibility and structural integrity. Drawing on this robust bioinorganic coordination, it is anticipated that these biological capping layers provide excellent long-term protection against environmental degradation. Consistent with this, previous research has shown that such protein capping can maintain the stability of biosynthesized QDs in liquid suspension for several months.[39] The TG data also demonstrate that the ZnS core and its ligand shell remain highly stable up to 300 °C, validating the reliability of subsequent surface characterizations.

BET characterization shows how this structural stability translates into textural properties. All five samples exhibit type IV adsorption−desorption isotherms with H2-type hysteresis loops (Figure 6b,c), a signature of mesoporous materials. The corresponding pore-size distributions (Figure 6d) are concentrated mainly in the 2−17 nm range. This can be attributed to the interparticle voids generated by the packing of near-spherical nanoparticles.[40,41] The specific surface areas (Table 2) highlight

Table 2. Results of BET Specific Surface Area (S_{BET}), Pore Volume, and Pore Diameter of Control-LB-ZnS, SBX-LB-ZnS, Control-TB-ZnS, SBX-TB-ZnS, and None-ZnS

samples	S_{BET} ($m^2 \cdot g^{-1}$)	pore volume ($cm^3 \cdot g^{-1}$)	pore diameter (nm)
Control-LB-ZnS	221.9496	0.5304	9.5590
SBX-LB-ZnS	268.0593	0.5976	8.9171
Control-TB-ZnS	185.7836	0.4439	9.5572
SBX-TB-ZnS	219.9209	0.4488	8.1626
None-ZnS	148.2005	0.1510	4.1902

a clear trend: EPS-directed synthesis substantially increases S_{BET} relative to the template-free control (None-ZnS, 148.20 $m^2 \cdot g^{-1}$), and SBX-induced stress amplifies this enhancement. SBX-LB-ZnS and SBX-TB-ZnS reach remarkably high values of 268.06 and 219.92 $m^2 \cdot g^{-1}$, respectively.

This enhancement is in agreement with the conformational unfolding mechanism described in Section 3.2.3. The network consisting of β-sheets and random coils acts as a loose, porous scaffold,[42] which spatially isolates the nucleating ZnS nanocrystals. Such steric confinement helps prevent the aggregation of primary particles into larger solid clusters, thereby preserving a high density of mesopores and active sites. For example, in this study, SBX-LB-ZnS exhibited a much higher S_{BET} than SBX-TB-ZnS. This coincides well with the secondary structure result: LB-EPS had the lowest α-helix/(β-sheet + random coil) ratio, which favored the formation of a more open and expansive spatial configuration. In contrast, the relatively more rigid structure of TB-EPS leads to a slightly denser particle packing. Collectively, SBX-LB-ZnS exhibited the highest S_{BET}, highlighting its optimized potential for applications in photocatalysis, sensing, and other nanomaterial fields.[43]

3.3.4. Correlation between the Protein Secondary Structure and ZnS QD Properties. Building upon the results in Section 3.2.3, this section extends the exploration of the structure−performance relationship between EPS protein secondary structure and the properties of the biosynthesized ZnS QDs. Figure 7 presents the correlation analysis between the α-helix/(β-sheet + random coil) ratio of Control-LB-ZnS, SBX-LB-ZnS, Control-TB-ZnS, and SBX-TB-ZnS and key ZnS QD metrics: yield, fluorescence intensity, polydispersity index (PDI), and specific surface area (S_{BET}).

The results reveal a distinct dichotomy in how EPS properties regulate QD synthesis. There is a strong correlation between the protein secondary structure and certain physical properties of QDs. Specifically, the α-helix/(β-sheet + random coil) ratio displayed high coefficients of determination with PDI (R^2 = 0.9327) and specific surface area (R^2 = 0.7632). A strong positive correlation was observed with PDI, indicating that a lower ratio directly leads to a lower PDI. A strong negative correlation with S_{BET} indicates that a lower ratio correlates with a

https://doi.org/10.1021/acs.biomac.6c00016
Biomacromolecules XXXX, XXX, XXX−XXX

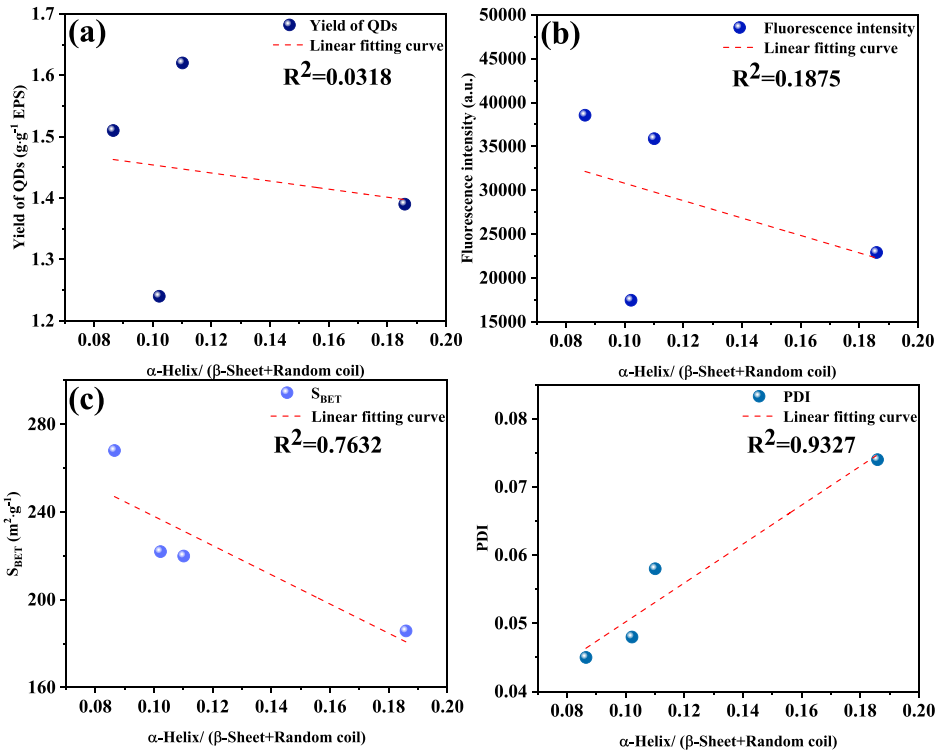

Figure 7. Correlation analysis between the [α-helix/(β-sheet + random coil)] ratio and the key properties of the biosynthesized ZnS QDs. The relationship is shown for (a) the QD yield, (b) fluorescence intensity, (c) specific surface area (S_{BET}), and (d) PDI.

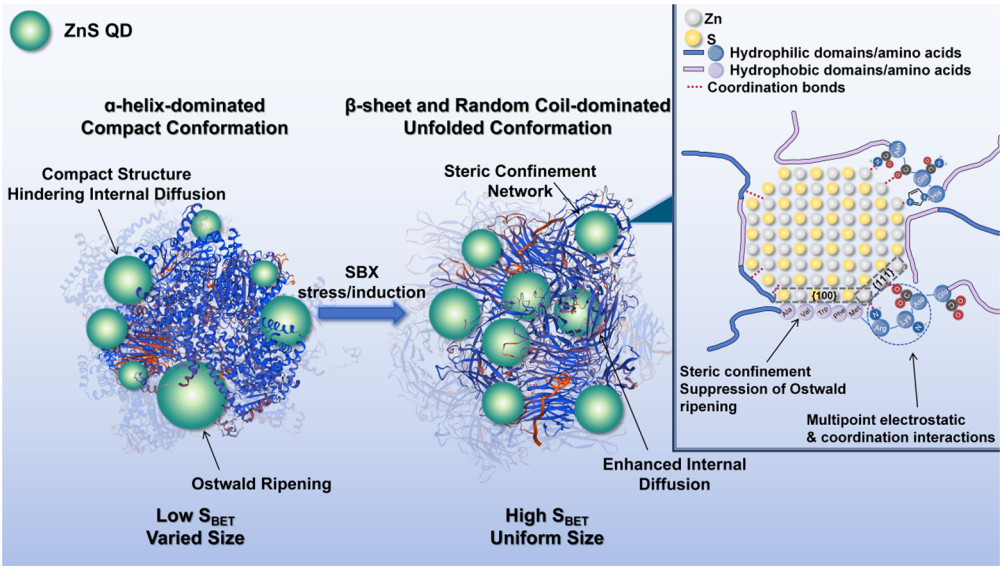

Figure 8. Schematic illustration of the conformational templating mechanism for the ZnS QD biosynthesis.

greater specific surface area. In contrast, the correlations with the QD yield ($R^2 = 0.0318$) and fluorescence intensity ($R^2 = 0.1875$) were notably weaker. This indicates that while structural conformation dictates morphological quality, the yield is predominantly controlled by the chemical abundance of metal-binding groups. This chemical abundance varies significantly between the LB-EPS and TB-EPS fractions.[3] Similarly, the weaker correlation observed for fluorescence intensity reflects that this optical property is comprehensively coregulated by multiple factors. These include the total QD yield, which is governed by functional groups, and size uniformity, which is governed by protein structure.[14]

Figure 8 schematically illustrates the proposed mechanistic origin of this structure−performance relationship. The significant association between the protein secondary structure and QD properties suggests a critical role of the EPS matrix as a physical template. When the proportion of α-helix decreases while the content of β-sheet and random coil increases, the proteins undergo conformational remodeling, adopting a loose and flexible structure.[42] Although this unfolding leads to the exposure of previously buried hydrophobic domains, it concurrently liberates and reorients the hydrophilic coordinating groups. This structural remodeling maximizes the accessibility and uniform positioning of these metal-binding sites,

https://doi.org/10.1021/acs.biomac.6c00016
Biomacromolecules XXXX, XXX, XXX−XXX

thereby constructing a spatially ordered "ligand mesh". This open architecture significantly enhances the diffusion of Zn(II) ions into the EPS matrix, achieving uniform preimmobilization of metal ions prior to the subsequent sulfidation and nucleation reactions.

Upon the introduction of S^{2-}, these homogeneously distributed precursor sites are hypothesized to induce a rapid nucleation event resembling a "burst nucleation" process. From the perspective of nucleation kinetics, this behavior is conceptually consistent with the framework of the LaMer nucleation model. This rapid process effectively narrows the nucleation window relative to the growth stage.[44] More critically, the exposed hydrophobic domains and the β-sheet-rich network can form a cage-like physical barrier, serving as a robust steric confinement effect. This steric hindrance restricts mass transfer between particles, thereby suppressing Ostwald ripening (the spontaneous process where small crystals dissolve to feed larger ones) more effectively than chemical adsorption alone.[45] Characterized by the lowest α-helix/(β-sheet + random coil) ratio, SBX-10-LB-EPS likely provided the most ideal physical template for synchronous nucleation and confined growth. Consequently, this optimal templating endowed the material with the narrowest particle size distribution and the lowest PDI.

To elucidate the specific binding interactions within this confined growth, a proposed facet-selective adsorption mechanism at the microinterface is depicted in the inset of Figure 8. This mechanism is based on the interfacial assembly model described by Bakshi.[46] In this framework, the hydrophilic and charged domains consist of polar side-chain residues (e.g., −COOH and $-NH_2$) and main-chain C=O groups liberated from α-helix hydrogen bonding.[25] These domains are hypothesized to preferentially coordinate onto the high-energy, highly polar {111} facets[47] of the β-ZnS nanocrystals via multipoint interactions. Conversely, the newly exposed hydrophobic domains favorably passivate the lower-energy, less polar {100} facets to minimize contact with the aqueous phase.

This study demonstrates that manipulating the protein structure of EPS is as crucial as modulating its chemical composition for the biosynthesis of high-quality nanomaterials.

4. CONCLUSIONS

This study demonstrates that flotation reagents, especially SBX, act as efficient "nongenetic regulators" that play a critical role in tailoring *S. oneidensis* MR-1 EPS for ZnS QD biosynthesis. SBX stress triggered a series of synergistic modifications. Beyond increasing EPS yield and enriching metal-binding functional groups, it drove a profound conformational transition from a rigid α-helix to a flexible β-sheet and random coil.

Further comparative analysis also indicated that there was a functional difference between LB-EPS and TB-EPS in the biosynthesis of QDs. LB-EPS, possessing the most unfolded conformation, served as a superior physical template for quality enhancement. This expanded spatial network enables an efficient, uniform adsorption reaction (i.e., preimmobilization). Furthermore, the resulting steric imprisonment likely enhances synchronous burst nucleation, while effectively suppressing Ostwald ripening. This structural advantage yielded QDs with superior size uniformity and a larger specific surface area. Conversely, although TB-EPS attained a greater QD yield, its more rigid structure failed to regulate the particle morphology as effectively. Correlation analysis further solidified these insights, demonstrating that QD physical properties (size distribution and specific surface area) strongly depend on the α-helix/(β-sheet + random coil) ratio, while the yield is predominantly controlled by chemical composition. In addition, it was observed that the change in the fluorescence intensity was synergistically controlled by the protein secondary structure and chemical composition.

Overall, this work proposes a novel strategy utilizing environmental stressors for the in situ engineering of the biophysical state of microbial EPS. This conformational regulation principle has strong universality; any external stress/induction conditions, such as other organic pollutants, heavy metals, or even pH and temperature changes that can effectively alter the amino acid composition of EPS as reported in previous literature, may induce favorable structural remodeling of biopolymers, thereby achieving similar control over the properties of nanomaterials. Consequently, this research offers a fresh understanding of the importance of transforming heavy metal pollutants into high-value nanomaterials. The proposed mechanism reveals that conformational control of the biological template strongly influences the morphology and performance of the QDs. This concept will play a crucial role in advancing both environmental cleanup and sustainable nanomaterial technologies.

Furthermore, it is important to acknowledge that the current proposed model is primarily based on protein-dominated EPS. For EPS where polysaccharides constitute the major component, the interfacial templating mechanisms and subsequent QD regulatory behaviors may differ. Nevertheless, drawing upon the physical principles elucidated in this study, it is reasonable to hypothesize that inducing a looser, more expanded architecture in polysaccharide chains could similarly enhance spatial confinement and mass transfer, thereby improving the overall quality of the synthesized QDs. Future systematic investigations into these polysaccharide-dominated EPS are warranted to fully uncover the diverse biomineralization mechanisms within complex biological matrices, thereby paving the way for more tailored and comprehensive biosynthesis strategies.

■ ASSOCIATED CONTENT

Supporting Information

The Supporting Information is available free of charge at https://pubs.acs.org/doi/10.1021/acs.biomac.6c00016.

Zn(II) concentrations in the supernatants from the first, second, and fourth centrifugation times of SBX-LB-ZnS and SBX-TB-ZnS (Figure S1) (PDF)

■ AUTHOR INFORMATION

Corresponding Authors

Weifeng Song − *Guangdong Key Laboratory of Environmental Catalysis and Health Risk Control, Guangdong Education Department Key Laboratory of Resources Comprehensive Utilization and Cleaner Production, School of Environmental Science and Engineering, Guangdong University of Technology, Guangzhou 510006, China;* orcid.org/0000-0002-9315-5145; Email: weifengsong@gdut.edu.cn

Wencan Dai − *Guangdong Key Laboratory of Environmental Catalysis and Health Risk Control, Guangdong Education Department Key Laboratory of Resources Comprehensive Utilization and Cleaner Production, School of Environmental Science and Engineering, Guangdong University of Technology, Guangzhou 510006, China; School of Environmental and*

https://doi.org/10.1021/acs.biomac.6c00016
Biomacromolecules XXXX, XXX, XXX−XXX

Chemical Engineering, Zhaoqing University, Zhaoqing 526061, China; Email: daiwencan168@163.com

Authors

Jingfeng Peng − *Guangdong Key Laboratory of Environmental Catalysis and Health Risk Control, Guangdong Education Department Key Laboratory of Resources Comprehensive Utilization and Cleaner Production, School of Environmental Science and Engineering, Guangdong University of Technology, Guangzhou 510006, China*; orcid.org/0009-0002-5483-4265

Zuoyi Yang − *Guangdong Key Laboratory of Environmental Catalysis and Health Risk Control, Guangdong Education Department Key Laboratory of Resources Comprehensive Utilization and Cleaner Production, School of Environmental Science and Engineering, Guangdong University of Technology, Guangzhou 510006, China*

Junming Bian − *Guangdong Key Laboratory of Environmental Catalysis and Health Risk Control, Guangdong Education Department Key Laboratory of Resources Comprehensive Utilization and Cleaner Production, School of Environmental Science and Engineering, Guangdong University of Technology, Guangzhou 510006, China*

Weixiong Lin − *School of Environmental and Chemical Engineering, Zhaoqing University, Zhaoqing 526061, China*

Xiaohui Zhou − *Guangdong Key Laboratory of Environmental Catalysis and Health Risk Control, Guangdong Education Department Key Laboratory of Resources Comprehensive Utilization and Cleaner Production, School of Environmental Science and Engineering, Guangdong University of Technology, Guangzhou 510006, China*

Keqin Zhou − *Guangdong Key Laboratory of Environmental Catalysis and Health Risk Control, Guangdong Education Department Key Laboratory of Resources Comprehensive Utilization and Cleaner Production, School of Environmental Science and Engineering, Guangdong University of Technology, Guangzhou 510006, China*

Chuanying Tu − *Guangdong Key Laboratory of Environmental Catalysis and Health Risk Control, Guangdong Education Department Key Laboratory of Resources Comprehensive Utilization and Cleaner Production, School of Environmental Science and Engineering, Guangdong University of Technology, Guangzhou 510006, China*

Guangwen Zheng − *Guangdong Key Laboratory of Environmental Catalysis and Health Risk Control, Guangdong Education Department Key Laboratory of Resources Comprehensive Utilization and Cleaner Production, School of Environmental Science and Engineering, Guangdong University of Technology, Guangzhou 510006, China*

Ziheng Song − *Guangdong Experimental High School, Guangzhou 510055, China*

Xiangdan Zhang − *Guangdong Key Laboratory of Environmental Catalysis and Health Risk Control, Guangdong Education Department Key Laboratory of Resources Comprehensive Utilization and Cleaner Production, School of Environmental Science and Engineering, Guangdong University of Technology, Guangzhou 510006, China*

Xiaoyan Bai − *Guangdong Key Laboratory of Environmental Catalysis and Health Risk Control, Guangdong Education Department Key Laboratory of Resources Comprehensive Utilization and Cleaner Production, School of Environmental Science and Engineering, Guangdong University of Technology, Guangzhou 510006, China*

Complete contact information is available at: https://pubs.acs.org/10.1021/acs.biomac.6c00016

Author Contributions

J.P.: writing − original draft, validation, software, methodology, investigation, formal analysis, and data curation. Z.Y.: writing − review and editing, resources, project administration, and methodology. W.S.: writing − review and editing, resources, project administration, methodology, conceptualization, and funding acquisition. W.D.: writing − review and editing, resources, project administration, methodology, and funding acquisition. J.B.: software, formal analysis, and data curation. W.L.: software, resources, and data curation. X. Zhou: software, formal analysis, and data curation. K.Z.: software, formal analysis, and data curation. C.T.: software, formal analysis, and data curation. G.Z.: software, formal analysis, and data curation. Z.S.: software, formal analysis, and data curation. X. Zhang: resources and data curation. X.B.: resources and data curation.

Notes

The authors declare no competing financial interest.

■ ACKNOWLEDGMENTS

This work was supported by the National Natural Science Foundation of China (grant number 42277220) and the Natural Science Foundation of Guangdong Province, China (grant number 2021A15150558). The authors extend their gratitude to Ms. Yu Wenqing(from Scientific Compass www.shiyanjia.com) for providing invaluable assistance with the BET analysis.

■ REFERENCES

(1) Molina, G. C.; Cayo, C. H.; Rodrigues, M. A. S.; Bernardes, A. M. Sodium Isopropyl Xanthate Degradation by Advanced Oxidation Processes. *Miner. Eng.* **2013**, *45*, 88−93.

(2) Natarajan, K. A.; Sabari Prakasan, M. R. Biodegradation of Sodium Isopropyl Xanthate by Paenibacillus polymyxa and Pseudomonas putida. *Min. Metall. Explor.* **2013**, *30* (4), 226−232.

(3) Peng, J.; Yang, Z.; Song, W.; Dai, W.; Bian, J.; Lin, W.; Leng, Z.; Zhou, K.; Tu, C.; Zheng, G.; Zhang, X.; Bai, X. The Stress/Induction Effects of Typical Flotation Reagents on Shewanella oneidensis MR-1: Spatial Distribution, Chemical Composition, and Zn(II) Adsorption Performance of Extracellular Polymeric Substances. *Biochem. Eng. J.* **2026**, *226*, No. 109966.

(4) Ye, F.; Jing, Y. Y.; Guo, S. W.; Yu, G. F.; Fan, Q. M.; Qu, F. F.; Gao, L.; Yang, Y.; Wu, D.; Meng, Y.; Yu, F. H.; Wei, L. X. Proliferative Ductular Reactions Correlate With Hepatic Progenitor Cell and Predict Recurrence in HCC Patients After Curative Resection. *Cell Biosci.* **2014**, *4* (1), 50.

(5) Lin, H.; Zhang, M.; Wang, F.; Meng, F.; Liao, B.-Q.; Hong, H.; Chen, J.; Gao, W. A Critical Review of Extracellular Polymeric Substances (EPSs) in Membrane Bioreactors: Characteristics, Roles in Membrane Fouling and Control Strategies. *J. Membr. Sci.* **2014**, *460*, 110−125.

(6) Gupta, P.; Diwan, B. Bacterial Exopolysaccharide Mediated Heavy Metal Removal: A Review on Biosynthesis, Mechanism and Remediation Strategies. *Biotechnol Rep. (Amst)* **2017**, *13*, 58−71.

(7) Chen, Y.; Wang, Q.; Zha, T.; Min, J.; Gao, J.; Zhou, C.; Li, J.; Zhao, M.; Li, S. Green and Facile Synthesis of High-Quality Water-Soluble Ag-In-S/ZnS Core/Shell Quantum Dots With Obvious Bandgap and Sub-Bandgap Excitations. *J. Alloys Compd.* **2018**, *753*, 364−370.

(8) Taylor, J. M.; Konda, A.; Morin, S. A. Spatiotemporal Control of Calcium Carbonate Nucleation Using Mechanical Deformations of Elastic Surfaces. *Soft Matter* **2020**, *16* (26), 6038−6043.

(9) Li, R.; Tang, L.; Zhao, Q.; Teng, K. S.; Lau, S. P. Facile Synthesis of ZnS Quantum Dots at Room Temperature for Ultra-Violet Photodetector Applications. *Chem. Phys. Lett.* **2020**, *742*, No. 137127.

(10) Xiao, X.; Ma, X. B.; Yuan, H.; Liu, P. C.; Lei, Y. B.; Xu, H.; Du, D. L.; Sun, J. F.; Feng, Y. J. Photocatalytic Properties of Zinc Sulfide Nanocrystals Biofabricated by Metal-Reducing Bacterium Shewanella oneidensis MR-1. *J. Hazard Mater.* **2015**, *288*, 134−139.
(11) Xu, L.-X.; Wang, Y.-Z.; Zhou, D.; Chen, M.-Y.; Yang, X.-J.; Ye, X.-M.; Yong, Y.-C. Bio-Metabolism-Driven Crystalline-Engineering of CdS Quantum Dots for Highly Active Photocatalytic H2 Evolution. *ChemistrySelect* **2021**, *6* (15), 3702−3706.
(12) Lee, S. H.; Jun, B.-H. Silver Nanoparticles: Synthesis and Application for Nanomedicine. *Int. J. Mol. Sci.* **2019**, *20* (4), 865.
(13) Chen, L.; Huang, X.; Yang, Z.; Song, W.; Wu, Z.; Li, J.; Tu, C.; Zheng, G.; Zhang, X.; Bai, X. Ammonium Salt Stress-Dependent Compositional Alteration in EPS From Desulfovibrio desulfuricans Subsp. desulfuricans and Its Mediating Role in PbS QDs Biosynthesis. *Chem. Eng. J.* **2025**, *512*, No. 162360.
(14) Huang, X.; Yang, Z.; Dai, W.; Song, W.; Gan, Y.; Lian, Z.; Zhou, W.; Wu, Z.; Chen, L.; Bai, X. Mediated Biosynthesis of CdS QDs by EPS From Desulfovibrio desulfuricans subsp. Under Carbon Source-Induced Reinforcement. *J. Hazard Mater.* **2023**, *459*, No. 132146.
(15) Wang, W.; Yan, Y.; Zhao, Y.; Shi, Q.; Wang, Y. Characterization of Stratified EPS and Their Role in the Initial Adhesion of Anammox Consortia. *Water Res.* **2020**, *169*, No. 115223.
(16) Mohammadi, F.; Sahihi, M.; Bordbar, A. K. Multispectroscopic and Molecular Modeling Studies on the Interaction of Two Curcuminoids With β-Lactoglobulin. *Spectrochim. Acta A Mol. Biomol. Spectrosc.* **2015**, *140*, 274−282.
(17) Guo, Q.; Li, S.; Yin, B.; Zhang, X.; Leng, Z.; Huang, Y.; Lin, W.; Yan, P.; Dai, W.; Sun, S. Target-Metal Stress-Induced Synthesis of Extracellular Polymeric Substances by Pseudomonas putida Enhances the Adsorption of Trace Platinum and Palladium from Wastewater. *Sep. Purif. Technol.* **2026**, *387*, No. 136646.
(18) Zheng, L.; Ding, A. Z.; Wang, J. S.; Tian, Y. Adsorption of Cd(II) and Zn(II) by Extracellular Polymeric Substances Extracted From Waste Activated Sludge. *Water Sci. Technol.* **2008**, *58* (1), 195−200.
(19) Murphy, J. M.; Powell, B. A.; Brumaghim, J. L. Stability Constants of Bio-Relevant, Redox-Active Metals With Amino Acids: The Challenges of Weakly Binding Ligands. *Coord. Chem. Rev.* **2020**, *412*, No. 213253.
(20) Giachini, L.; Francia, F.; Veronesi, G.; Lee, D.-W.; Daldal, F.; Huang, L.-S.; Berry, E. A.; Cocco, T.; Papa, S.; Boscherini, F.; Venturoli, G. X-Ray Absorption Studies of Zn2+ Binding Sites in Bacterial, Avian, and Bovine Cytochrome bc1 Complexes. *Biophys. J.* **2007**, *93* (8), 2934−2951.
(21) Ojemaye, M. O.; Okoh, O. O.; Okoh, A. I. Uptake of Zn2+ and As3+ from Wastewater by Adsorption onto Imine Functionalized Magnetic Nanoparticles. *Water* **2018**, *10* (1), 36.
(22) Su, X.; Cui, W.; Zhang, Z.; Zhang, J.; Zhou, H.; Zhou, K.; Xu, Y.; Wang, Z.; Xu, B. Effects of L-Lysine and L-Arginine on the Structure and Gel Properties of Konjac Glucomannan. *Food Hydrocoll.* **2023**, *137*, No. 108404.
(23) Argos, P.; Hanei, M.; Garavito, R. M. The Chou-Fasman Secondary Structure Prediction Method With an Extended Data Base. *FEBS Lett.* **1978**, *93* (1), 19−24.
(24) Cheng, P. N.; Pham, J. D.; Nowick, J. S. The Supramolecular Chemistry of β-Sheets. *J. Am. Chem. Soc.* **2013**, *135* (15), 5477−5492.
(25) Kabsch, W.; Sander, C. Dictionary of Protein Secondary Structure: Pattern Recognition of Hydrogen-Bonded and Geometrical Features. *Biopolymers* **1983**, *22* (12), 2577−2637.
(26) Hong, P.-N.; Taing, C.; Phan, P.-T.; Honda, R. Polarity-Molecular Weight Profile of Extracellular Polymeric Substances in a Membrane Bioreactor: Comparison between Bulk Sludge and Cake Layers. *J. Water Environ. Technol.* **2018**, *16* (1), 40−53.
(27) Lian, J.; Yang, Y.; Qiu, W.; Huang, L.; Wang, C.; Chen, Q.; Ke, Q.; Wang, Q. Fluorescent Characteristics and Metal Binding Properties of Different Molecular Weight Fractions in Stratified Extracellular Polymeric Substances of Activated Sludge. *Separations* **2021**, *8* (8), 120.
(28) Wang, J.; Li, Q.; Li, M.-M.; Chen, T.-H.; Zhou, Y.-F.; Yue, Z.-B. Competitive Adsorption of Heavy Metal by Extracellular Polymeric Substances (EPS) Extracted From Sulfate Reducing Bacteria. *Bioresour. Technol.* **2014**, *163*, 374−376.
(29) Wei, D.; Li, M.; Wang, X.; Han, F.; Li, L.; Guo, J.; Ai, L.; Fang, L.; Liu, L.; Du, B.; Wei, Q. Extracellular Polymeric Substances for Zn(II) Binding During Its Sorption Process Onto Aerobic Granular Sludge. *J. Hazard Mater.* **2016**, *301*, 407−415.
(30) Yue, L.; Qi, S.; Wang, J.; Cai, J.; Xin, B. Controllable Biosynthesis and Characterization of α-ZnS and β-ZnS Quantum Dots: Comparing Their Optical Properties. *Mater. Sci. Semicond. Process.* **2016**, *56*, 115−118.
(31) Siddik, A.; Satheesh, S. Characterization and Assessment of Barnacle Larval Settlement-Inducing Activity of Extracellular Polymeric Substances Isolated From Marine Biofilm Bacteria. *Sci. Rep.* **2019**, *9* (1), 17849.
(32) Summers, H. D.; Holton, M. D.; Rees, P.; Williams, P. M.; Thornton, C. A. Analysis of Quantum Dot Fluorescence Stability in Primary Blood Mononuclear Cells. *Cytometry, Part A* **2010**, *77* (10), 933−939.
(33) Krishna, P. H.; Ramrakhiani, M. Effect of Particle Size Distribution on Spectral Characteristics of Different Quantum Dots. *Int. J. Appl. Eng. Res.* **2018**, *13* (3), 1722−1727.
(34) Soltani, N.; Saion, E.; Erfani, M.; Rezaee, K.; Bahmanrokh, G.; Drummen, G. P. C.; Bahrami, A.; Hussein, M. Z. Influence of the Polyvinyl Pyrrolidone Concentration on Particle Size and Dispersion of ZnS Nanoparticles Synthesized by Microwave Irradiation. *Int. J. Mol. Sci.* **2012**, *13* (10), 12412−12427.
(35) Ghoderao, K. P.; Jamble, S. N.; Sawant, J. P.; Kale, R. B. Solution-Assisted Growth Mechanism and Characterization of ZnS Microspheres. *Mater. Res. Express* **2017**, *4* (2), No. 025026.
(36) Hussain, M.; Zahoor, T.; Akhtar, S.; Ismail, A.; Hameed, A. Thermal Stability and Haemolytic Effects of Depolymerized Guar Gum Derivatives. *J. Food Sci. Technol.* **2018**, *55* (3), 1047−1055.
(37) Weiss, I. M.; Muth, C.; Drumm, R.; Kirchner, H. O. K. Thermal Decomposition of the Amino Acids Glycine, Cysteine, Aspartic Acid, Asparagine, Glutamic Acid, Glutamine, Arginine, and Histidine. *BMC Biophys.* **2018**, *11* (1), 2.
(38) Lu, D.; Ran, Y.; Wang, W.; Huang, Y. Developing Adjustable Micro- and Mesopore Structured Carbon Materials From Wood via Biotechnology for Enhanced Capacitive Deionization. *Chem. Eng. J.* **2024**, *500*, No. 157043.
(39) Abou-Assy, R. S.; El-Deeb, B. A.; Al-Talhi, A. D.; Mostafa, N. Y. Biosynthesis of Cadmium Selenide Quantum Dots by Providencia vermicola. *Afr. J. Microbiol. Res.* **2019**, *13* (6), 106−121.
(40) Gholamrezaei, S.; Ghiyasiyan-Arani, M.; Salavati-Niasari, M.; Moayedi, H. Multidisciplinary Methods (Co-Precipitation, Ultrasonic, Microwave, Reflux and Hydrothermal) for Synthesis and Characterization of CaMn3O6 Nanostructures and Its Photocatalytic Water Splitting Performance. *Int. J. Hydrogen Energy* **2019**, *44* (48), 26373−26386.
(41) Dutta, A.; Mondal, J.; Patra, A. K.; Bhaumik, A. Synthesis and Temperature-Induced Morphological Control in a Hybrid Porous Iron−Phosphonate Nanomaterial and Its Excellent Catalytic Activity in the Synthesis of Benzimidazoles. *Chem. - Eur. J.* **2012**, *18* (42), 13372−13378.
(42) Hou, X.; Liu, S.; Zhang, Z. Role of Extracellular Polymeric Substance in Determining the High Aggregation Ability of Anammox Sludge. *Water Res.* **2015**, *75*, 51−62.
(43) Liu, D.; Nyakuchena, J.; Maity, R.; Geng, X.; Mahajan, J. P.; Hewa-Rahinduwage, C. C.; Peng, Y.; Huang, J.; Luo, L. Quantum dot gels as efficient and unique photocatalysts for organic synthesis. *Chem. Commun.* **2022**, *58* (80), 11260−11263.
(44) Thanh, N. T. K.; Maclean, N.; Mahiddine, S. Mechanisms of Nucleation and Growth of Nanoparticles in Solution. *Chem. Rev.* **2014**, *114* (15), 7610−7630.
(45) Gommes, C. J. Ostwald Ripening of Confined Nanoparticles: Chemomechanical Coupling in Nanopores. *Nanoscale* **2019**, *11* (15), 7386−7393.
(46) Bakshi, M. S. Nanoshape Control Tendency of Phospholipids and Proteins: Protein−Nanoparticle Composites, Seeding, Self-

https://doi.org/10.1021/acs.biomac.6c00016
Biomacromolecules XXXX, XXX, XXX−XXX

Aggregation, and Their Applications in Bionanotechnology and Nanotoxicology. *J. Phys. Chem. C* **2011**, *115* (29), 13947−13960.
(47) Zscheckel, T.; Wisniewski, W.; Rüssel, C. Polarity Controlled Epitaxial Growth of 111-Layers in CVD-ZnS Proven by EBSD. *Mater. Charact.* **2022**, *185*, No. 111770.

NOTE ADDED AFTER ASAP PUBLICATION

Figure 4 was corrected on April 23, 2026.

https://doi.org/10.1021/acs.biomac.6c00016
Biomacromolecules XXXX, XXX, XXX−XXX